Dynamic Modeling of a Multiple Hearth Furnace for Kaolin Calcination

Aleksi Eskelinen, Alexey Zakharov, and Sirkka-Liisa Jämsä-Jounela
Dept. of Biotechnology and Chemical Technology, School of Chemical Technology, Aalto University, FI-00076
Espoo, Finland

Jonathan Hearle
Imerys Minerals Par Moor Center, Par Moor Road, Par PL24 2SQ, England

DOI 10.1002/aic.14903

A dynamic model of a multiple hearth kaolin calciner has been developed and is presented in this article. This model describes the physical-chemical phenomena taking place in the six furnace parts: the solid phase, gas phase, walls, cooling air, rabble arms, and the central shaft. The solid phase movement, in particular, is described by a novel mixing model. The mixing model divides the solid bed in a hearth into volumes and the distribution of their contents, after one full central shaft rotation, is identified by the pilot experiments. First, the model is validated by the industrial data, and then the dynamics of the multiple hearth furnace is studied by introducing step changes to the three manipulated variables: the feed rate, and the gas, and air flows supplied. The responses of the gas phase temperature and solid bed component profiles are analysed and the results are discussed. © 2015 American Institute of Chemical Engineers *AIChE J*, 61: 3683–3698, 2015

Keywords: multiple hearth furnace (MHF), dynamic modeling, kaolin calcination, pilot experiments, industrial application, parameter estimation

Introduction

Multiple hearth furnaces (MHF) are widely used in industry for the calcination of clay minerals, such as kaolin.[1] Calcination enhances the properties of kaolin ensuring its applicability for a wide variety of products, such as paper, rubber, paint, and refractory items.[2] However, mineral processing continues to provide challenges particularly in the area of maintaining efficient process operations.[3] Specifically, growing global competition in the mineral processing industry has increased the need for higher grade products. To improve the quality of calcined kaolin, more knowledge is needed on the solid temperature profile inside the furnace[4] and on the physicochemical phenomena occurring during calcination. Mechanistic models have proven to be an excellent tool for gaining deeper understanding of processes and their behavior.[5–7] The development of mechanistic models is supported by the numerous studies of the reactions related to kaolin calcination. For example, the fundamentals of kaolin calcination and classification of different calcined kaolin grades have been previously introduced in Murray.[2,8] Furthermore, the kinetics of kaolin calcination was examined by Ptacek et al.,[9,10] while both Langer[11] and Castelein et al.[12] have analyzed the influence of the heating rate on the properties of calcined kaolin. Additionally, industrial experiments with tracer materials were used to study the residence time distribution in the furnaces used for calcination, such as the MHF[1] and rotary kilns.[13,14]

Despite the abundance of research examining the calcination reactions, significant research is still required to quantitatively describe the phenomena occurring in the MHF calciner. In the literature, several mathematical models with necessary elements have been reported. Meisingset and Balchen[15] developed a steady-state mechanistic model for a single hearth rotary coke calciner, which outlined mass and energy balance equations for the coke bed, gas phase, and the lining. Martins et al.[16] described a one-dimensional steady-state model of the petroleum coke calcination in a rotary kiln that predicts the temperature profiles for the bed, gas phase, and the kiln wall in the axial direction. Additionally, it also predicted the composition profiles for the gas and solid phase. The model included rheological characteristics of the system of particles for modeling the axial flow of the bed. Voglauer and Jörgl[17] presented a dynamic model of a multiple hearth furnace used for the roast process to recover vanadium consisting of a mass transfer model, thermodynamic model, and a chemical model for the characterization of decisive states like mass, temperatures and the concentrations of sodium, and soluble and insoluble vanadium, respectively. Liu and Jiang[18] have also developed a mathematical model involving the mass and heat transfer in a continuous plate dryer. The authors presented equations to calculate the key parameters of the solid mass transfer model, such as the height and the volume of each granular heap, and retention time in the dryer. The study showed that the optimization of a plate dryer should

---

Correspondence concerning this article should be addressed to A. Zakharov at alexey.zakharov@aalto.fi

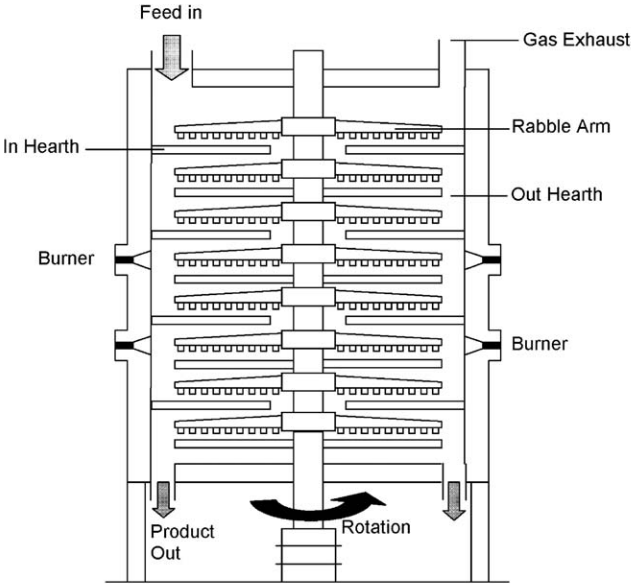

Figure 1. Cross-sectional picture of the multiple hearth furnace with direct fire burners.

concentrate on maximizing the effective covering ratio of the plates. More recently, Ginsberg and Modigell[19] developed a dynamic model of a rotary kiln used for the calcination of titanium dioxide. The overall heat transfer phenomena and the reactions occurring in the process were described. The model was validated by a dynamic test case representing a 15-day period of plant operation and the work succeeded in proving that the dynamic behaviour of a furnace can be modelled with quantitative accuracy.

The aim of this article is to present the development of the dynamic model describing kaolin calcination in a MHF operated by a UK plant. In the model, the solid bed in a hearth is divided into volumes, as presented earlier by Meisingset and Balchen,[15] as the temperature difference through a solid bed in a hearth is over 150°C. The solid phase movement, particularly, is described by a novel mixing model which offers a simple and computationally efficient way to describe the solid dynamics. In addition to dividing the solid bed in a hearth into volumes, the mixing model provides the distribution of their contents, after one full central shaft rotation, identified by the pilot experiments. The pilot experiments were not conducted in the abovementioned modelling papers, even though they provide the essential information regarding the residence time distribution of the solid phase between different hearths, which is necessary to properly describe the phenomena taking place in the furnace. The research outlined here is part of a project aiming at the development of model-based state estimation, monitoring, and control of the furnace, based on the knowledge of the physical-chemical phenomena taking place in the process. In fact, the implementation of advanced control of the furnace plays the key role in improving the final product quality. This article comprises of the following. First, the kaolin calcination process in a MHF is described in Section Description of Kaolin Calcination in a Multiple Hearth Furnace, while Section Dynamic Model of a Multiple Hearth Furnace presents the physical and chemical relationships for the calcination reactions, and the equations for the heat and mass transfer phenomena within the furnace. Section Calculating Model Parameters from the Experimental Data introduces the experimental work used to determine the parameters of the calcination reactions and the mixing model. Section Estimation of Parameters and Model Validation introduces the estimation of the model parameters that cannot be calculated from the physical-chemical laws and also reports the steady-state temperature and solid bed composition profiles and presents the model validation results. In Section Dynamic Behavior of the MHF, the dynamic behaviour of the MHF model is analysed and finally, Section Conclusions concludes the article.

Description of Kaolin Calcination in a Multiple Hearth Furnace

The MHF studied in this article consists of eight hearths and it has counter-current solid and gas flows. The heat required for calcination is supplied to the furnace through four tangentially aligned methane burners located on Hearths 4 and 6. The temperature in the "fired hearths" is controlled by varying the fuel gas flow, which determines the amount of combustion air. The furnace walls are constructed of bricks and enclosed by a cylindrical steel shell with refractory lining. Figure 1 presents the cross-sectional view of the furnace.

The material flow through the furnace is stirred spirally and moved across the hearths by a centrally located vertical rotating shaft carrying arms with rabble blades. Four arms are used on each hearth, and each arm carries three to five rabble blades, while material is fed into the top hearth through a single inlet from the weigh feed hopper to the periphery of the hearth. On the odd numbered hearths, the material is stirred by the rabble blades toward the centre of the hearth, and the material drops down to the next hearth from the centre through a single annulus around the shaft. In contrast, the material on the even numbered hearths is moved outward to be dropped through the drop holes at the periphery of the hearth to the following hearth. The stirring pattern is repeated until the lowest hearth is reached, from which the calcined product is extracted through the two exit holes.

During calcination, kaolin undergoes four physical-chemical processes presented in Ref. 9. First the evaporation of the free moisture occurs ($T \leq 100°\text{C}$)

$$\mathrm{H_2O(l)} \rightarrow \mathrm{H_2O(g)} \tag{1}$$

Next, kaolin undergoes a dehydroxylation reaction, in which the chemically bound water is removed and amorphous metakaolin is formed at 450–700°C

$$\mathrm{Al_2O_3 \cdot 2SiO_2 \cdot 2H_2O} \rightarrow \mathrm{Al_2O_3 \cdot 2SiO_2} + \mathrm{2H_2O(g)} \tag{2}$$

The third physical-chemical process involves a reaction leading to the transformation of metakaolin to the "spinel phase" by exothermic recrystallization at 925–1050°C.

$$\mathrm{2(Al_2O_3 \cdot 2SiO_2)} \rightarrow \mathrm{2Al_2O_3 \cdot 3SiO_2} + \mathrm{SiO_2(amorphous)} \tag{3}$$

In the fourth and final process, the nucleation of the spinel phase occurs and the material transforms into mullite at temperatures above 1050°C

$$\mathrm{3(2Al_2O_3 \cdot 3SiO_2)} \rightarrow \mathrm{2(3Al_2O_3 \cdot 2SiO_2)} + \mathrm{5SiO_2} \tag{4}$$

Mullite is hard and abrasive, and as a result it can cause damage to process equipment.[4] The desired final consistent product which is within the specification limits has both a low mullite and metakaolin content. The differential scanning calorimetry (DSC) and thermo gravimetric (TGA) curves presenting the kaolin calcination are given in Figure 2.

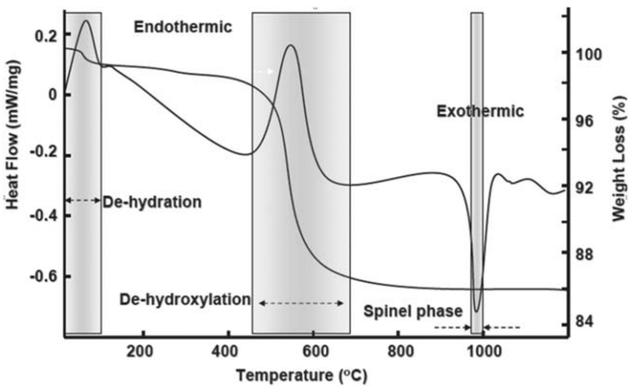

Figure 2. DSC and TG curves of kaolin.

Dynamic Model of a Multiple Hearth Furnace

In this modeling work, the MHF is divided to six parts: the solid bed, gas phase, walls, central shaft, rabble arms, and the cooling air. The overall mathematical model of the furnace includes the reaction kinetics for the four reactions outlined earlier, as well as models for the mass transfer and heat transfer mechanisms for each of six parts. In addition, equations for calculating the temperature dependent parameters, such as the heat capacities of the gas components, the gas emissivities, and the solid bed emissivities, are incorporated in the model. The solid bed and the gas phase both have five components: the solid bed includes kaolin, water, metakaolin, spinel phase (product), and mullite (offspec), whereas the gas phase includes methane, oxygen, nitrogen, water, and carbon dioxide. The first three subsections present the modeling equations and then Subsection Solution procedure for the MHF model introduces a summary of the solving procedure.

Modeling of the calcination reactions and methane combustion

The four reactions presented in Eqs. 1–4 occur in the solid bed and the reaction rate R_i of each reaction is described by the Arrhenius equation $\left(R_i = k_i C_i = A_i e^{-\frac{E_{A,i}}{RT}} C_i\right)$. The frequency factors and activation energies of each reaction are selected by fitting the reaction rate curves to the DSC and TGA curves of kaolin, as further explained in Section Determination of the reaction parameters.

The burning of methane is assumed to be incomplete proximal to the burners and the heat provided is distributed along the gas phase in the hearths. Equation 5 presents the combustion reaction of methane

$$\mathrm{CH_4(g)+2O_2(g) \rightarrow CO_2(g)+2H_2O(g)} \tag{5}$$

The amount of combustion energy ($\Delta H_{\mathrm{combust}}$) that the reaction provides is given by the lower heating value of 802 kJ/mol.

Modeling of solids and gas phase mass transfer

A few simplifying assumptions have to be made to model the mass transfer inside the furnace. First, the solid bed on each hearth is split into 4 (Hearths 3 to 8) or 5 (Hearths 1 and 2) homogenous annular volumes according to the furnace rabble arm configuration. Second, the volumes are assumed to be identical in width in the radial direction and the mass content. Third, the mixing model assumes that one full shaft rotation distributes the contents of a volume between the original volume and its neighbor volumes (one of which is the next and the other is the previous). The distribution of solid among the three volumes is determined by the experimental tests which are described in Section Determination of the solid bed movement matrix D and in addition, the density of the solids is assumed to remain constant. Under these assumptions, it is proposed in this work to calculate the solid mass distribution after one time step (representing a full central shaft rotation) with Eq. 6

$$m^j_{t+1} = D_j \cdot \left(m^j_t \text{-} R^j_{r,t}\right) + m^j_{\mathrm{feed},t} \tag{6}$$

where the mass movement matrix D describes the distribution of the contents of each compartment m^j_t after one central shaft rotation in the hearth j, $R^j_{r,t}$ and $m^j_{\mathrm{feed},t}$ denote the mass loss in the solid phase in Hearth j and the feed to the Hearth in one central shaft rotation. Specifically, the column i represents the distribution of volume i between the volumes of the hearth. In other words, element D_{ji} is the share of content of volume i moving to volume j in one central shaft rotation. Thus, the columns of the matrix sum up to unity, except the column representing the exit volume of the hearth. Moreover, because of the assumption that solids in a certain volume are distributed between the current volume and its neighbor volumes after one rotation, the matrix D has three nonzero central diagonals. Thus, the central diagonal represents the contents staying in the same volume, whereas the upper and lower diagonals indicate the proportion of solid moving inward and outward, respectively. Recalling Eq. 6, the feed to a hearth can be found as the exit from the previous one as follows

$$m^j_{\mathrm{feed},t} = \left(1 - \Sigma D^K_{j-1}\right)\left(m^{j-1,K}_t - R^{j-1,K}_{r,t}\right) \tag{7}$$

where K is the exit volume of hearth $j-1$ and D^K_{j-1} is the column K of matrix D_{j-1}.

The solid bed movement matrix is generated for each hearth individually. As an example, it is proposed in this work to define the solid bed movement matrix of the upmost hearth according to Eq. 8. The parameter α is introduced to describe the net forward flow through a hearth, which is the feed rate minus the mass loss caused by evaporation and dehydroxylation reactions. The upper diagonal matrix elements a_1 present the full forward flow from the current volume to the next volume during one full central shaft rotation. Thus, the lower diagonal matrix elements ($a_1 - \alpha$) present the backward flow equal to the difference of the full forward and the net forward flows. In Eq. 8, the parameter α is only present in the second and third volume since the feed is introduced to volume 4 and the direction of flow is in the descending order of volumes on the first hearth

$$D_1 = \begin{matrix} 1-a_1 & a_1 & 0 & 0 & 0 \\ a_1-\alpha & 1-2\ a_1+\alpha & a_1 & 0 & 0 \\ 0 & a_1-\alpha & 1-2\ a_1+\alpha & a_1 & 0 \\ 0 & 0 & a_1-\alpha & 1-2\ a_1 & a_1 \\ 0 & 0 & 0 & a_1 & 1-a_1 \end{matrix} \tag{8}$$

The gas phase in the model is assumed to be ideal and the pressure inside the furnace atmospheric. As was the case with the solid bed, also the gas phase on a specific hearth is divided into 4 or 5 homogenous annular volumes, with the number of gas phase volumes in the hearth the same as the corresponding number of solid volumes in the hearth. Additionally, the gas phase volumes are assumed to be uniform regarding composition and temperature. The gas phase has a very short residence time in the furnace, and its temperature follows the steady-state values defined by the temperature profiles of the other model parts, allowing, the gas phase to be described with a steady-state model.

The gas phase mass balance equation (Eq. 9) is derived for each primary gas component

$$\dot{n}_{i,\mathrm{in}}-\dot{n}_{i,\mathrm{out}}-R_i=0 \tag{9}$$

where $n_{i,\mathrm{out}}$ denotes the amount of moles of component i leaving a volume, R_i is the mass change of component i due to reactions, and $n_{i,\mathrm{in}}$, denoting the incoming moles of component i, is obtained from Eq. 10

$$n^j_{i,\mathrm{in}}=c_i^{j+1}F^j \tag{10}$$

where j is the number of the volume, F_j is the gas flow through the hearth, and c_i^{j+1} is the concentration of component i in the previous volume.

The total gas flow in Hearths 7 and 8 is equal to the draft through the drop holes at the bottom hearth. The total gas flow in Hearths 5 and 6 comprises of the combustion gas and air fed to Hearth 6 as well as the gases from evaporation and dehydroxylation, and the air flow from the previous hearth. The total gas flow at Hearths 1 to 4 consists of the gas flow from Hearth 5, the combustion gas and air fed to Hearth 4 and the gases from evaporation and dehydroxylation. The real volumetric gas flow, F_{real}, on each hearth having different temperature can be calculated according to the ideal gas law as

$$F_{\mathrm{real}}=F_{\mathrm{NTP}}\frac{T_{\mathrm{real}}}{T_{\mathrm{NTP}}} \tag{11}$$

where F_{NTP} is the volumetric flow computed assuming the atmospheric temperature and pressure.

Modeling of the energy balances

In the model, the heat exchange is described between solid and gas, solid and wall, gas and wall, wall and environment, and gas and arms. In addition, heat is conducted inside the walls in the radial horizontal direction and heat exchange exists between the cooling air, the central shaft, and the rabble arms. In the model, heat exchange between the hearth bottom surface and the solid bed, and heat conduction inside the solid bed are neglected. Furthermore, the bed volumes are assumed to be homogenous in temperature. The model considers energy balances for the gas phase, walls, the central shaft, rabble arms, cooling air, and for the solid bed. The energy balance equations, containing the heat flows, are first resolved after which the temperature values can be acquired. The energy balance equation for the gas phase is

$$\dot{Q}_{\mathrm{gas,in}}-\dot{Q}_{\mathrm{gas,out}}+\dot{Q}_{\mathrm{combustion}}+\dot{Q}_{\mathrm{gs}}+\dot{Q}_{\mathrm{gw}}+\dot{Q}_{\mathrm{gshaft}}+\dot{Q}_{\mathrm{garms}}=0 \tag{12}$$

where $\dot{Q}_{\mathrm{gas,in}}$ and $\dot{Q}_{\mathrm{gas,out}}$ denote the enthalpy of the incoming and the outgoing gas flows, $\dot{Q}_{\mathrm{combustion}}$ is the energy released by the combustion, and the last four terms in the left side of Eq. 12 represent the heat exchange of the gas phase with the solid, walls, central shaft and the arms.

The molar heat capacities of the incoming and exiting gas components are calculated as a function of temperature as previously outlined in Ref. 20. The combustion energy is calculated using Eq. 13

$$\dot{Q}_{\mathrm{combustion}}=b_i\dot{n}_{\mathrm{methane}}\Delta H_{\mathrm{combust}} \tag{13}$$

where b_i is an estimated combustion ratio, which is described in more detail in Section Estimation of Parameters and Model Validation, n_{methane} denotes the methane feed rate, and $\Delta H_{\mathrm{combust}}$ is the specific enthalpy of the methane combustion.

The direct heat transfer between the solid bed and the gas phase $\dot{Q}_{\mathrm{gs}}$ occurs by both radiation and convection

$$\dot{Q}_{\mathrm{gs}}=\sigma X_{\mathrm{s}}A_{\mathrm{gs}}\varepsilon_{\mathrm{s}}\varepsilon_{\mathrm{g}}\left(T_{\mathrm{g}}^4-T_{\mathrm{s}}^4\right)+h_{\mathrm{cgs}}X_{\mathrm{s}}A_{\mathrm{gs}}\left(T_{\mathrm{g}}-T_{\mathrm{s}}\right) \tag{14}$$

where σ is the Stefan-Boltzmann constant, A_{gs} is the area of the Hearth bottom. The calculation of the solid and gas emissivity ε_{s} and ε_{g} is described in Section Solid bed and gas phase emissivity and the determination of the heat transfer coefficient h_{cgs} is presented in Supporting Information Appendix A, which also describes the calculation of all the other heat exchange coefficients. X_{s} is an estimated surface view factor, which is outlined further in Section Estimation of Parameters and Model Validation.

Heat transfer between the inner walls and the gas phase $\dot{Q}_{\mathrm{gw}}$ occurs by convection and radiation and the heat flux can be written as in Meisingset and Balchen[15]

$$\dot{Q}_{\mathrm{gw}}=\sigma A_{\mathrm{gw}}\frac{(\varepsilon_{\mathrm{w}}+1)}{2}\varepsilon_{\mathrm{g}}\left(T_{\mathrm{g}}^4-T_{\mathrm{w}}^4\right)+h_{\mathrm{cgw}}A_{\mathrm{gw}}\left(T_{\mathrm{g}}-T_{\mathrm{w}}\right) \tag{15}$$

where σ is the Stefan-Boltzmann constant, A_{gw} is the area of the walls, ε_{w} and ε_{g} is the emmisivity of the walls and the gas, T_{g} and T_{w} is the temperature of the gas and the walls, and h_{cgw} is the heat transfer coefficient. The radiation term is written as described in Ref. 15 and the effective emissivity as presented in Ref. 21.

To calculate the heat transfer between the gas, the central shaft and the rabble arms, the central shaft is divided into eight sections according to the hearths, so that each section has a fixed temperature and there is no vertical heat exchange in the shaft. The heat exchange flux between the gas phase and the central shaft $\dot{Q}_{\mathrm{gshaft}}$, and between the gas phase and rabble arms $\dot{Q}_{\mathrm{garms}}$ consist of the radiative and the convective heat transfer terms, respectively

$$\begin{aligned}\dot{Q}_{\mathrm{gshaft}}=&\ \sigma ZA_{\mathrm{gshaft}}\varepsilon_{\mathrm{shaft}}\varepsilon_{\mathrm{g}}\left(T_{\mathrm{gas}}^4-T_{\mathrm{shaft}}^4\right)\\&+h_{\mathrm{cgshaft}}ZA_{\mathrm{gshaft}}\left(T_{\mathrm{gas}}-T_{\mathrm{shaft}}\right)\end{aligned} \tag{16}$$

$$\begin{aligned}\dot{Q}_{\mathrm{garms}}=&\ \sigma A_{\mathrm{garms}}\varepsilon_{\mathrm{arms}}\varepsilon_{\mathrm{g}}\left(T_{\mathrm{gas}}^4-T_{\mathrm{arms}}^4\right)\\&+h_{\mathrm{cgarms}}A_{\mathrm{garms}}\left(T_{\mathrm{gas}}-T_{\mathrm{arms}}\right)\end{aligned} \tag{17}$$

where σ is the Stefan-Boltzmann constant, A_{gshaft} and A_{garms} is the area of the central shaft and the arms, $\varepsilon_{\mathrm{shaft}}$, $\varepsilon_{\mathrm{arms}}$, and ε_{g} are the emissivity of the shaft, the arms and the gas, whereas T_{shaft}, T_{arms}, and T_{g} are the temperature of the respective model parts, h_{gshaft} and h_{arms} are the heat transfer coefficients, and Z is an estimated constant describing the insulation of the central shaft, which is further explained in Section Estimation of Parameters and Model Validation.

The energy balance equation for the walls is given by

$$\frac{\partial Q_{\mathrm{w}}}{\partial t}=\dot{Q}_{\mathrm{wg}}-\dot{Q}_{\mathrm{ws}}-\dot{Q}_{\mathrm{wa}} \tag{18}$$

where Q_{w} is the heat accumulated in the walls, and $\dot{Q}_{\mathrm{wg}}$ and $\dot{Q}_{\mathrm{wa}}$ denote the heat exchange between the walls and the gas, and the walls and the ambient air. The heat transfer between the solid bed and the walls $\dot{Q}_{\mathrm{ws}}$ occurs only by radiation since the two surfaces are not connected to each other. The radiative heat flux is computed according to Ginsberg and Modigell[19]

$$\dot{Q}_{\mathrm{ws}}=\sigma X_{\mathrm{s}} A_{\mathrm{sw}} \varepsilon_{\mathrm{sw}}\left(T_{\mathrm{w}}^{4}-T_{\mathrm{s}}^{4}\right) \tag{19}$$

where σ is the Stefan-Boltzmann constant, X_{s} and A_{sw} are the form factor of the solid surface and the area of the Hearth bottom, and the emissivity between the solid bed and the walls $\varepsilon_{\mathrm{sw}}$ is affected by the gas phase emissivity and its calculation is described in Supporting Information Appendix A. The heat transfer between the outer wall and the ambient air $\dot{Q}_{\mathrm{wa}}$ consists only of a convective term as the radiative term is neglected due to the relatively low outer wall temperature

$$\dot{Q}_{\mathrm{wa}}=h_{\mathrm{cwa}} A_{\mathrm{wa}}\left(T_{\mathrm{ambient}}-T_{\mathrm{outer\,wall}}\right) \tag{20}$$

where A_{wa} is the surface of the outer layer of the furnace wall, T_{ambient} and $T_{\mathrm{outer\,wall}}$ is the temperature of the ambient air and the outer layer of the wall, and h_{cwa} is the heat transfer coefficient. In order to describe the conductive heat transfer inside the wall and to calculate its temperature profile, the furnace wall is divided into eight sections according to the hearths, so that each section has an individual temperature and there is no vertical heat exchange in the wall. The calculation of the wall layer temperature is further discussed in Supporting Information Appendix A.

The equation describing the heat in the central shaft Q_{shaft} and the rabble arms Q_{arms} are provided by

$$\frac{\partial Q_{\mathrm{shaft}}}{\partial t}=\dot{Q}_{\mathrm{gshaft}}-\dot{Q}_{\mathrm{shaft,cool}} \tag{21}$$

$$\frac{\partial Q_{\mathrm{arms}}}{\partial t}=\dot{Q}_{\mathrm{garms}}-\dot{Q}_{\mathrm{arms,cool}} \tag{22}$$

where the heat exchange between the gas and the shaft and arms is denoted by $\dot{Q}_{\mathrm{gshaft}}$ and $\dot{Q}_{\mathrm{garms}}$, respectively. The heat transfer between cooling air and the central shaft $\dot{Q}_{\mathrm{shaft,cool}}$ and the rabble arms $\dot{Q}_{\mathrm{arms,cool}}$ consist of the radiative and the convective heat transfer terms, respectively

$$\begin{aligned}\dot{Q}_{\mathrm{shaft_{cool}}} &= \sigma A_{\mathrm{shaft_{cool}}} \varepsilon_{\mathrm{shaft}}\left(T_{\mathrm{shaft}}^{4}-T_{\mathrm{cool}}^{4}\right)\\ &\quad + h_{\mathrm{cshaft_{cool}}} A_{\mathrm{shaft_{cool}}}\left(T_{\mathrm{shaft}}-T_{\mathrm{cool}}\right)\end{aligned} \tag{23}$$

$$\begin{aligned}\dot{Q}_{\mathrm{arms_{cool}}} &= \sigma A_{\mathrm{arms_{cool}}} \varepsilon_{\mathrm{arms}}\left(T_{\mathrm{arms}}^{4}-T_{\mathrm{cool}}^{4}\right)\\ &\quad + h_{\mathrm{carms_{cool}}} A_{\mathrm{carms_{cool}}}\left(T_{\mathrm{arms}}-T_{\mathrm{cool}}\right)\end{aligned} \tag{24}$$

where σ is the Stefan-Boltzmann constant, $A_{\mathrm{shaft_{cool}}}$ and $A_{\mathrm{arms_{cool}}}$ are the area of the central shaft and the arms, $\varepsilon_{\mathrm{shaft}}$ and $\varepsilon_{\mathrm{arms}}$ is the emissivity of the shaft and the arms, whereas T_{shaft}, T_{arms}, and T_{cool} are the temperature of the respective model parts, $h_{\mathrm{cshaft_{cool}}}$ and $h_{\mathrm{carms_{cool}}}$ are the heat transfer coefficients.

The energy contents of the cooling air $Q_{\mathrm{cooling\,air}}$ is described by Eq. 25

$$\begin{aligned}\frac{\partial Q_{\mathrm{cooling\,air}}}{\partial t} &= \dot{Q}_{\mathrm{cooling\,air,in}}+\dot{Q}_{\mathrm{arms,cool}}+\dot{Q}_{\mathrm{shaft,cool}}\\ &\quad -\dot{Q}_{\mathrm{cooling\,air,out}}\end{aligned} \tag{25}$$

where $\dot{Q}_{\mathrm{cooling\,air,in}}$ and $\dot{Q}_{\mathrm{cooling\,air,out}}$ are the enthalpy of the cooling are entering and leaving the volume, whereas $\dot{Q}_{\mathrm{shaft,cool}}$ and $\dot{Q}_{\mathrm{arms,cool}}$ denote the heat exchange power between the cooling area and the central shaft and the arms, respectively.

Finally, the solid phase energy balance equation is written as

$$\frac{\partial Q}{\partial t}=\dot{Q}_{\mathrm{mass,in}}-\dot{Q}_{\mathrm{mass,out}}-\dot{Q}_{\mathrm{reactions}}-\dot{Q}_{\mathrm{evaporation}}+\dot{Q}_{\mathrm{sw}}+\dot{Q}_{\mathrm{sg}} \tag{26}$$

where Q denotes the enthalpy of the solid contents of a volume, $\dot{Q}_{\mathrm{mass,in}}$ and $\dot{Q}_{\mathrm{mass,out}}$ represent the energy in the solid entering and leaving the volume, $\dot{Q}_{\mathrm{reactions}}$ and $\dot{Q}_{\mathrm{evaporation}}$ describe the enthalpy of the chemical reactions taking place in the solid phase and free water evaporation, whereas the last two terms in Eq. 26 represent the heat exchange between the solid bed and the walls, and the solid bed and the gas. When considering the solid bed movement during one time step (one central shaft rotation), the energy in each solid bed compartment can be calculated using Eq. 27, in a similar way as previously outlined in Eq. 6

$$Q_{t+1}^{j,k}=D_{j}\cdot Q_{t}^{j,k}+Q_{\mathrm{feed},t} \tag{27}$$

For each component in the solid phase, the heat capacity is assumed to be constant, see Table 1.

Solid bed and gas phase emissivity. The solid bed consists of kaolin which consists mainly of a mixture of aluminium oxide and silicon oxide. The literature values for the emissivity of aluminium oxide and silicon oxide at various temperatures are given in Ref. 23–25. From them a correlation between the emissivity of the kaolin $\varepsilon_{solidbed}$ and the temperature $T_{solidbed}$ is determined (see Supporting Information Appendix B) and the derived result is given in Eq. 28

$$\varepsilon_{\mathrm{solidbed}}=2.10*10^{-7}*T_{\mathrm{solidbed}}^{2}-0.00064*T_{\mathrm{solidbed}}+0.88 \tag{28}$$

The gas emissivity in Hearths 1 to 6 is affected by the water and carbon dioxide content and the temperature of the gas phase. Other gas phase components are not considered as they all are small two atomic components and as such, do not affect the radiation properties of gas.[21] The gas phase in Hearths 7 and 8 is close to the air, having little content of water and carbon dioxide, and therefore, the emissivity can be estimated as 0.1–0.13 according to Ref. 21. However, this value is increased by the solid particle presence in the gaseous phase. Thus, it was decided to estimate the effective emissivity of the gaseous phase in Hearths 7 and 8 as 0.2, which allowed to achieve reasonably low temperature of the solid leaving the furnace. The gas phase emissivity, calculated according to Perry and Green[21] (Table 5.7), are summarized in Table 2.

Solution procedure for the MHF model

The developed model contains differential, algebraic and the difference (discrete-time) equations representing the mixing model, and therefore, a standard DAE (differential-algebraic equations) solver cannot be applied. Instead, a special solving algorithm has been tailored for the developed model taking into account the different time scales of the dynamics of the model parts. In more detail, the time step of the solver is naturally limited by one full central shaft rotation, which makes the first-order Euler method very accurate for describing the slow dynamics of the solid phase and the wall

Table 1. The Heat Capacities of the Solid Components

Component	Heat Capacity (kJ/kg K)	Reference
Water	4.18	Perry and Green[21]
Kaolin	1.16	Schieltz and Soliman[22]
Metakaolin	1.19	Schieltz and Soliman[22]
Spinel phase	0.93	Obtained experimentally in the plant
Mullite	1.11	Schieltz and Soliman[22]

temperature. Therefore, higher order methods, like Runge-Kutta are not required. Taking into account the slow dynamics of the solid phase and the wall temperature, the energy balance of the fast gaseous phase is resolved separately (before) computing the balance for the slower phases, which results in avoiding iterations and reducing computations. Furthermore, the gaseous phase has to be resolved after computing the solid phase mass balances, providing the amount of water transferred from the solid to the gas phase. Finally, computing the mass and energy flows between the model parts only ones per time step is necessary to achieve the mass and energy conservation in the solution, which is frequently even more important in practice than reaching a higher order of the solving procedure. In summary, the solving procedure presented in Figure 3 was developed utilizing theoretical considerations to avoid unnecessary iterations and higher-order solving procedures and as a result, the implemented solver is able to simulate a day of real time in about 2 min on an average PC.

The solution procedure for the MHF model consists of five main steps. First, the reaction rates are calculated using the reaction parameters obtained from the experimental data.

Table 2. The Calculated Gas Phase Emissivity

Hearth	1	2	3	4	5	6	7	8
ε	0.34	0.32	0.3	0.27	0.27	0.23	0.2	0.2

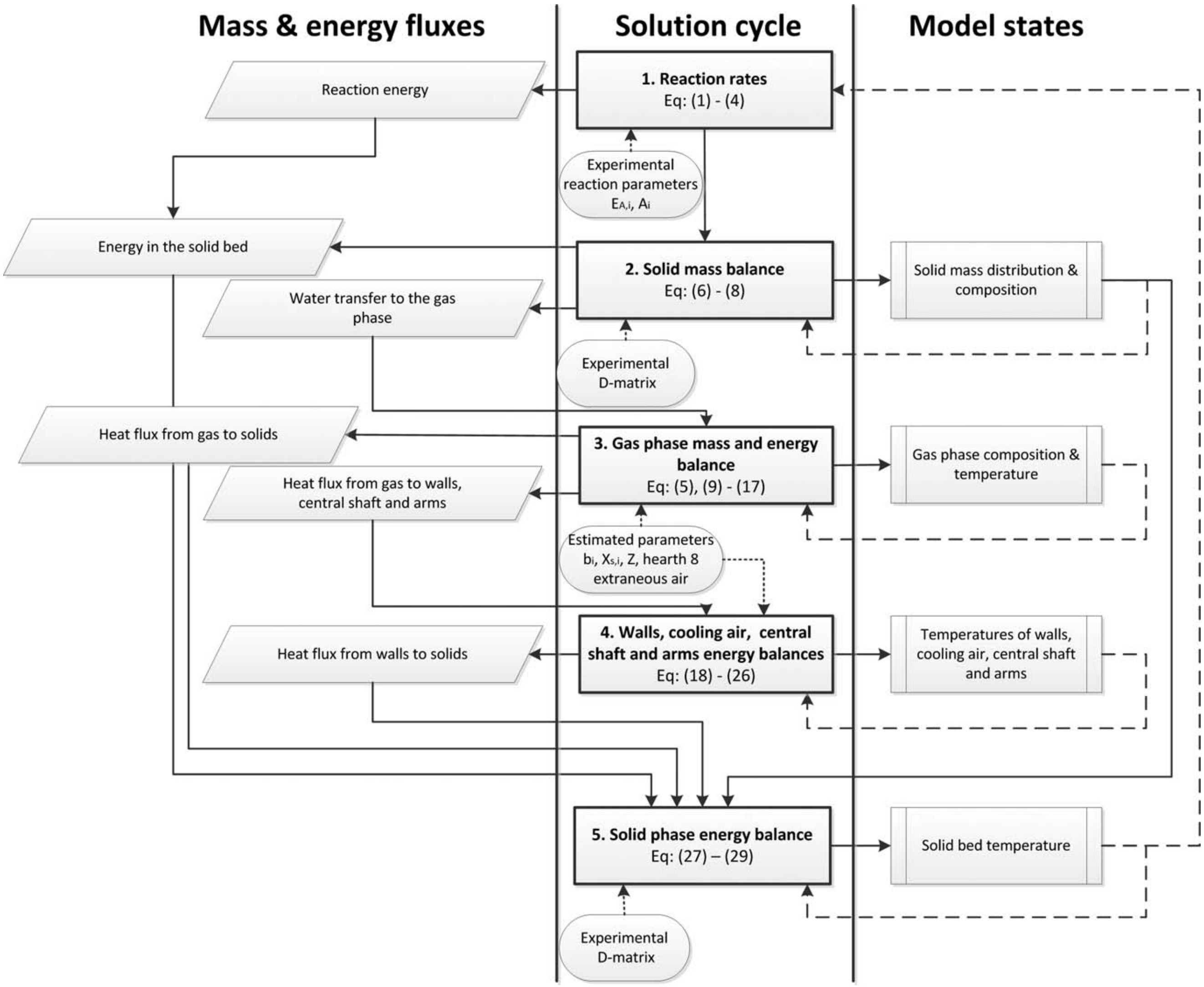

Figure 3. Scheme of the solution procedure for the MHF model.

Table 3. Reaction Parameters of the Four Reactions Occurring During Kaolin Calcination

Reaction	Frequency Factor (1/s)	Activation Energy (kJ/mol)	Kinetic Parameters Found in the Literature: Frequency Factor *A* (1/s) and Activation Energy *E* (kJ/mol)	Enthalpy of the Reaction (kJ/kg)
Evaporation	5×10^7	61.0	$A = 1.967 \times 10^4$, $E = 40.4$ (Lyons et al.[26])	2258.2
Dehydroxylation	1×10^7	145.0	$A = 2.83 \times 10^8$, $E = 157.1$ (Criado et al.[28]) $A = 8.33 \times 10^3$, $E = 108.9$ (Bellotto[27]) – disordered kaolin $A = 6.33 \times 10^6$, $E = 158.0$ (Bellotto[27]) – ordered kaolin $A = 9.57 \times 10^8$, $E = 196.8$ (Saikia et al.[29]) $A = 9.74 \times 10^{10}$, $E = 195$ (Ptacek et al.[10]), n = 2.24	891.0
Spinel formation	5×10^{33}	856.0	$E = 856$ (Ptacek et al.[9]) $E = 700 – 727$ (Silva et al.[30])	−212.9
Mullite formation	1×10^{17}	522.0	$A = 4.93 \times 10^{15}$, $E = 512.5$ (Ptacek et al.[31]), $\Theta > 6$ C/min $A = 1.83 \times 10^{13}$, $E = 525$ (Gualtieri et al.[32])	1301.7

Second, the solid mass balance is computed, which requires the mixing model. Third, the mass and energy balances of the gas phase are solved using the estimated parameters, such as the burning ratios, solid bed surface view factors and the extraneous air flow to Hearth 8. The next step consists of energy balance calculations for the walls, cooling air, central shaft, and the rabble arms. The fifth and final step solves the energy balance of the solid bed by combining the heat fluxes determined in the previous steps by utilizing the mixing model. The model solution cycle is presented in Figure 3 summarizing the mass and energy flows between the model parts and the usage of the current model states. In addition, Figure 3 shows in which step the experimentally determined and the estimated parameters are used in the calculations.

During one solution cycle, representing one full rotation of the central shaft, the solving procedure calculates the current states of the six model parts (the solid phase, gas phase, walls, cooling air, rabble arms, and the central shaft). The first step, the computation of the reaction rates in the solid phase, is done by direct calculations using the current temperature profile distribution. In the second step, the solid bed mass balance is solved using the computed reaction rates and the experimentally determined mixing model. After the first two steps, the energy produced by the reactions in the solid bed, the energy flows caused by the convection in the solid bed and the water transferred to the gas phase are available. In the next step, the water transferred to the gas phase is first used to calculate the mass balance, and subsequently the energy balance of the gas phase is determined. Specifically, the steady-state values of the heat fluxes between the gas phase and other model parts are calculated by solving algebraic equations achieved by an interval division method. Subsequently, the fourth step involves solving the temperature profiles of the walls, central shaft, rabble arms and the cooling air using the obtained heat fluxes. Finally, the last step of the solution cycle combines the heat fluxes in the solid bed, the heat exchange between the solid bed and other model parts, and the composition of the solid bed to calculate its energy balance and temperature profile through the furnace. In these last two steps, Euler's method is employed. The solving algorithms have been implemented in MATLAB environment. The solving procedure is developed to compute the mass and energy flows between the model parts once during a solution cycle. Thus, while resolving the balance equations of two model parts, the same value of the mass and heat flow between them is used. A conservative solution scheme is attained and the mass and energy conservation is achieved in the solution.

Calculating Model Parameters from the Experimental Data

Determination of the reaction parameters

The reaction parameters, namely the frequency factor and activation energy of the Arrhenius equation, were determined for the four reactions (Eqs. 1–4) by identifying the reaction rate curves from the experimental data provided by the company operating the furnace. The experimental reaction data obtained by using the DSC and TGA is shown in Figure 2. The reaction parameters were determined by approximating the reaction rate curves while using a heating rate of 40°C/min. Table 3 lists the obtained values of the kinetic parameters and the values of the reaction enthalpies, as well as the kinetics found in the literature.

Regarding the evaporation of free water, both Meisingset and Balchen[15] and Martins[16] refer to the kinetics defined by Lions et al.,[26] which are provided in Table 3. Assuming the constant heating rate of 40°C/min, these reaction kinetics and the kinetics used in this article result in a similar fraction of unreacted component, as confirmed by Figure 4.

The kinetics of the dehydroxilation reaction have been investigated by a number of authors, who have conducted numerous experiments at different temperature ranges and using kaolin samples with varying properties. Bellotto et al.[27] observed a significant difference between the kinetics of the dehydroxylation reaction for ordered and disordered kaolin samples. Moreover, the reaction rate obtained by Bellotto et al.[27] was 100 times slower when compared with the results of Criado et al.,[28] which was explained by the approximately 10 times larger particle size in the latter case. In addition, different model orders (first, second, and third) and kinetic mechanisms were employed in the literature to describe the kinetics at different conversion rates. As an example, Saikia et al.[29] compared nine options to describe the reaction at the temperature range between 450 and 600°C, and Ptacek et al.[10] estimated Avrami exponent as 2.24. As a result, the kinetic parameters obtained from the literature show a wide range of variation. In this article, the kinetics were selected to describe the experimental data provided by the plant. The obtained reaction rate is slower compared with the ones proposed by Criado et al.[28] However, Criado et al.[28] did not specify the degree of kaolin structural disorder and considered the experimental data up to the conversion rate of 0.6, which could cause

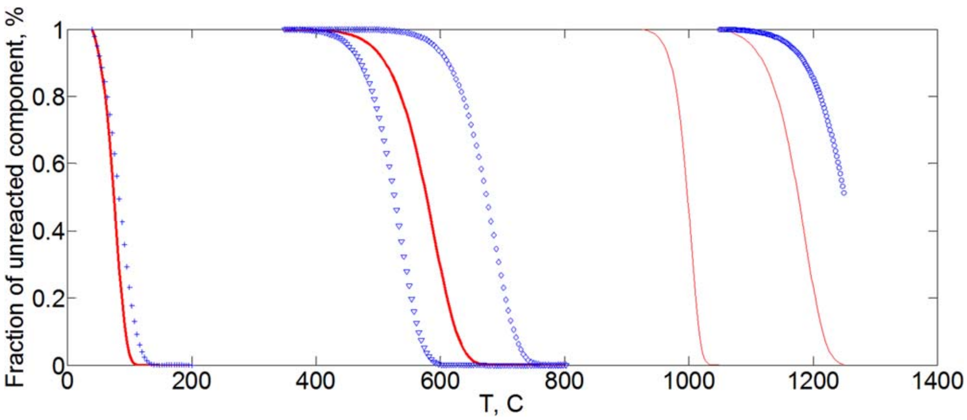

Figure 4. The fraction of unreacted components assuming the heating rate of 40 C/min.

Solid line denotes the reactions used in the present study, crosses – evaporation of water according to Lyons et al.,[26] triangles – dihydroxylation according to Criado et al.,[28] diamonds – dihydroxylation according to Saikia et al.[29] circles – mullite formation according to Ptacek et al.[9] [Color figure can be viewed in the online issue, which is available at wileyonlinelibrary.com.]

the difference in the obtained kinetic parameters. On the other hand, the reaction rate used in the present study is faster than the ones obtained by Bellotto et al.[27] and Saikia et al.[29]

With respect to the formation of spinel phase, the kinetics proposed by Ptacek et al.[9] are used in this article, as it agrees well with the experimental data provided by the plant. As an alternative, Silva et al.[30] obtained a slightly lower value for the activation energy (700 – 727 kJ).

The mullite formation reaction was studied by Ptacek et al.,[31] who concluded that the activation energy of the reaction depends on the heating rate Θ. According to these kinetics, mullite formation activates at a temperature above 1100°C, whereas the experimental results provided by the plant show that the reaction should start at around 1050°C. Therefore, the activation energy proposed by Ptacek et al.[31] was used to describe the reaction kinetics in this study, whereas the frequency factor was increased in order to fit the experimental data from the plant. Gualtieri et al.[32] obtained a similar value for the activation energy, however, the frequency factor value is lowered by a larger particle size in the samples used in the experiments. In addition, the effect of the kaolin structural order on the reaction kinetics has been confirmed in this study.

Determination of the solid bed movement matrix D

Material and methods. The main equipment used for the testing includes a pilot scale furnace and a continuous weight proportioner. The pilot scale multiple hearth furnace is a 1:12 ratio replica of the industrial furnace without heating equipment. The rabble arm configuration is the same as it is in the original multiple hearth furnace. The walls are made of Perspex allowing for the observation of the solid bed movement and an Engelhardt continuous weight proportioner is used as the feeder device. The feeding mechanism consists of rough and fine streams separated by a weighing pan with the desired feed rate can be entered to the feeder by accuracy of 10 grams per hour. The material is fed from the container to the rough feeding section. From there, the material is moved to the fine feeding section through a weighing pan which discharges the material to the fine feeding section in predetermined cycles. The cycle time is adjusted to the desired feed rate and it is calculated by the machine automatically.

The residence time distribution through the whole pilot furnace was studied using tracer experiments. Sesame and coriander seeds were used as the tracing materials, as the bulk density of the seeds is 592 kg/m^3 for sesame and 338 kg/m^3 for coriander, which is close to the bulk density of kaolin powder (350 kg/m^3). It was also noticed during the experiments that the seeds were carried with the clay powder and their flow pattern was similar.

The tracer experiments were executed using a feed rate of 70 g/min corresponding to the real feed rate of about 120 kg/min. The rotation speed of the central shaft was 3 RPM. The steps of the tracer experiments were the following: the pilot furnace was operated to steady state; tracer material (100 grams) was weighed and dosed into the pilot over one minute. Samples were collected from the two bottom drop holes; from the drop hole A samples were taken every 5 min for the first 20 min, and then every minute thereafter, while from the drop hole B, the samples were taken about every 7 min. After completing the sampling, the seeds were separated from the samples by sieving and weighted.

The mass distribution experiments were executed using a feed rate of 70 g/min corresponding to the real feed rate of about 120 kg/min. The rotation speed of the central shaft was 3 RPM. The steps of the mass distribution experiments were the following: the pilot furnace was operated to the steady state, and then feeder and the rabble arms of the pilot were stopped. The furnace was subsequently disassembled and the mass of the material on each hearth was weighed.

Experimental results and the determination of the solid bed moving matrices. The movement of the solid bed was studied to determine the residence time of every hearth. The

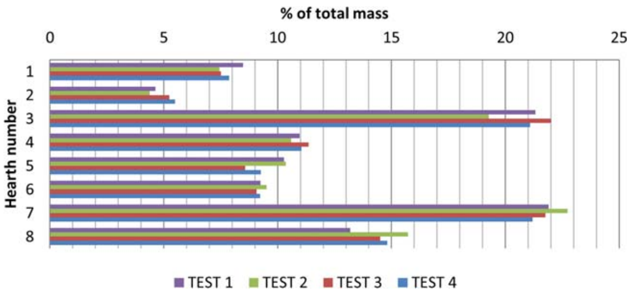

Figure 5. Mass distribution between the hearths from the tests 1, 2, 3, and 4.

[Color figure can be viewed in the online issue, which is available at wileyonlinelibrary.com.]

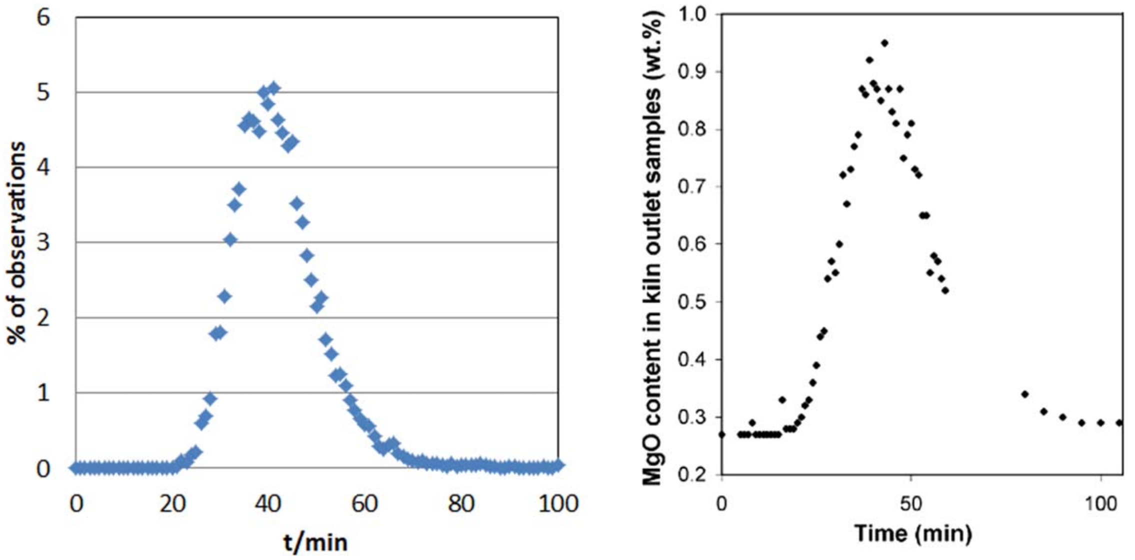

Figure 6. The residence time distribution according to the mixing model matrices (left) and the tracer content in the product during the industrial experiments[1] (right).

[Color figure can be viewed in the online issue, which is available at wileyonlinelibrary.com.]

mass distribution between the hearths was studied with a pilot furnace. The shape of the residence time distribution estimated from the pilot experiments fits perfectly to the distribution obtained by industrial experiments.[1] However, even if proper scaling has been selected, the mean residence time obtained from the pilot experiments is slightly shorter compared to the mean residence time measured in the plant. Therefore, the residence time distribution obtained from the experiments with the real plant has been utilized to estimate the mixing matrix. Subsequently, using the residence time distribution for the whole furnace and the mass distribution between the hearths, the solid movement matrices were defined.

The mass distributions obtained in the four experiments performed are shown in Figure 5. Clearly, Hearths 3 and 7 have the largest portions of kaolin, whereas Hearths 1 and 2 have the smallest portions indicating that the material spends a relatively short time on the first two hearths and a much longer time on Hearths 3 and 7. The results of the four tests showed a good correlation and are shown in Figure 5.

The net forward flow coefficients α_j, used in the solid bed movement matrix, were chosen to achieve consistency between the experimental results and the mixing model prediction of the mass distribution between the hearths and the residence time distribution. The backward flow parameters a_j were selected to be 5% of the total net flow for Hearths 1 and 2, and 10% for the rest of the other hearths, since higher values of the backward flow in the first two hearths are inconsistent with the short residence time in these particular hearths.

Table 4. The Burning Ratios

		Volume			
		1	2	3	4
Hearth	4	$b_1 \times (1 - b_1)^3$	$b_1 \times (1 - b_1)^2$	$b_1 \times (1 - b_1)$	b_1
	5	$b_2 \times (1 - b_2)^4$	$(1 - b_2)^5$	0	0
	6	$b_2 \times (1 - b_2)^3$	$b_2 \times (1 - b_2)^2$	$b_2 \times (1 - b_2)$	b_2

Figure 6 presents the resulting residence time distribution according to the identified solid movement model and shows the residence time distribution curve of the industrial experiment. Comparison between the model and the industrial setting shows that both of the curves are consistent. Additionally, in both cases, the tracer starts reaching the outlet approximately 20 min after introduction into the system and the last particles leave the furnace within 80 min.

Estimation of Parameters and Model Validation

Four different types of model parameters introduced in Eqs. 13, 14, 16, and 19 need to be determined from the experimental data. These four parameters are:

1. The burning ratios b_i (at Hearths 4, 5, and 6 as shown in Table 4) distributing the combustion energy obtained between the different volumes, are identified from the process data. The burning ratios are used for simplification of the complex fluid dynamics calculation in the presence of combustion flame. In fact, if all of the methane would be burned in the volume next to the walls its temperature would increase too high.

2. Form and view factors $X_{s,i}$ for the solid bed surface areas, which describe the surface shape of the solid bed and it is used to follow the energy transfer between the gas and solid phases in each hearth i.

3. The central shaft has insulation, but its characteristics are unknown. If the insulation is ignored in the model, the

Table 5. The Steady-State Inputs and Outputs used for Model Adaptation

Variable	Value
Feed rate	120 kg/min
Gas flow H4	3.684 kg/min
Air flow to H4	69.857 kg/min
Gas flow to H6	2.219 kg/min
Air flow to H6	39.69 kg/min
Cooling air flow	88.0 kg/min
Cooling air exit temperature	160°C
Product exit temperature	750°C

Table 6. Values of the Estimated Model Parameters

Parameter	b_1	b_2	$X_{s,1}$	$X_{s,2}$	$X_{s,3}$	$X_{s,4}$	$X_{s,5}$	$X_{s,6}$	$X_{s,7}$	$X_{s,8}$	Z	Extraneous air to H8 (kg/min)
Value	0.77	0.5	0.52	0.46	1.9	1.34	1.39	0.5	1.28	0.56	0.72	34.78

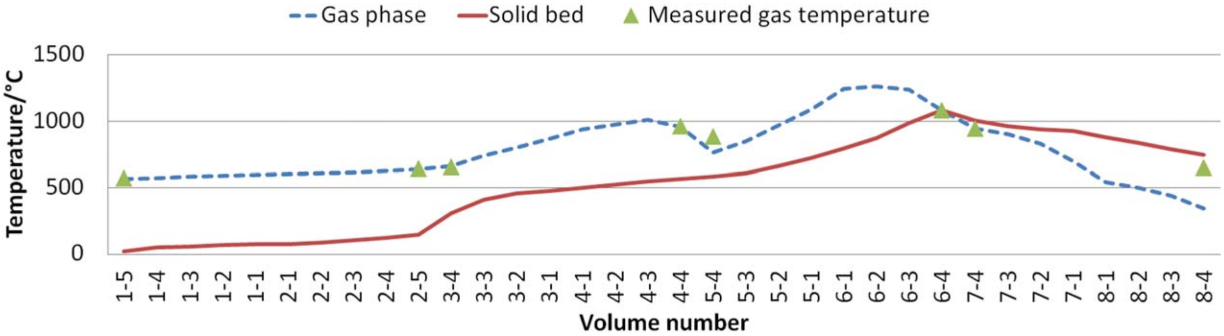

Figure 7. The steady-state temperature profile of the MHF at the feed rate of 120 kg/h.

The *x*-axis presents the volumes of the solid and the gas phases organised in the order of the solid flow from top to bottom. [Color figure can be viewed in the online issue, which is available at wileyonlinelibrary.com.]

cooling air temperature increases to an unrealistically high value. Therefore, a heat exchange area multiplier Z is introduced to lower the heat exchange between the central shaft and the gas phase and between the rabble arms and the gas phase. The multiplier Z can be estimated from the energy the cooling air absorbs from the furnace since the amount of the cooling air and its inlet and exit temperatures are known.

4. Extraneous air flow to Hearth 8 through the bottom drop holes is unknown. This extraneous air flow is introduced for cooling down the solid bed in Hearths 7 and 8, since no other mechanisms for cooling are available. Specifically, it is known that the solid bed reaches temperature up to 1050°C at the end of Hearth 6 and the solids exit the furnace at a temperature around 750°C. This information can be used to estimate the amount of the extraneous air flow. In addition, it was confirmed from the operative personnel at the plant that there a draft through the drop holes exists.

For determination of these model parameters, the steady-state process data from May 2013, at which the feed rate was 120 kg/min, was used. The steady values of the input variables and the outputs (the exit temperature of the cooling air and the product) are summarized in Table 5.

Next, the model parameters were estimated by minimizing the sum of the mass and energy balance errors and the errors between the model outputs and the actual measurement data. Specifically, the modeling error minimization procedure was conducted utilizing nonlinear least-squares as shown in Eq. 29

$$\min_{x,\ p} \left(f_1(x)^2 + f_2(x)^2\right) \tag{29}$$

where p contains the burning ratios, form factors, insulation multiplier and the extraneous air flow to Hearth 8, x represents a model steady state, f_1 denotes the error of the mass and energy balances and f_2 is the error between the output variables of the state x and the actual measured variables. The estimated model parameters are given in Table 6.

The estimated parameter values were applied and a simulation at the steady state was performed. The resulting temperature profiles of the solid bed and of the gas phase predicted by the model are presented in Figure 7 with the measured values of the gas phase temperatures next to the walls.

Figure 7 shows that in Hearths 1 and 2, the solids temperature rises to 170°C and only the evaporation of free moisture occurs. This is because of the short residence time on these

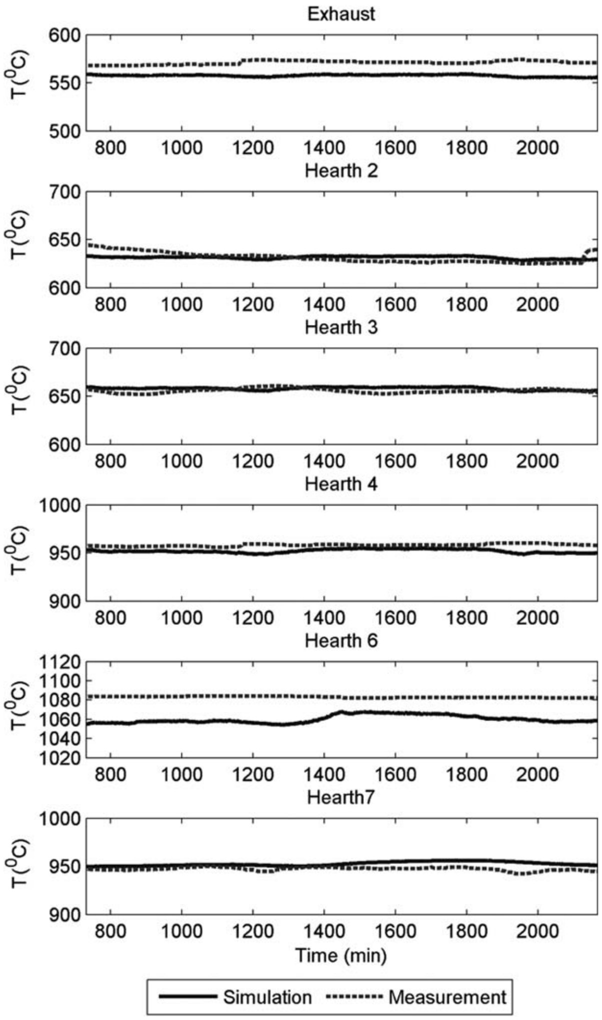

Figure 8. The model simulation compared with industrial measurement data.

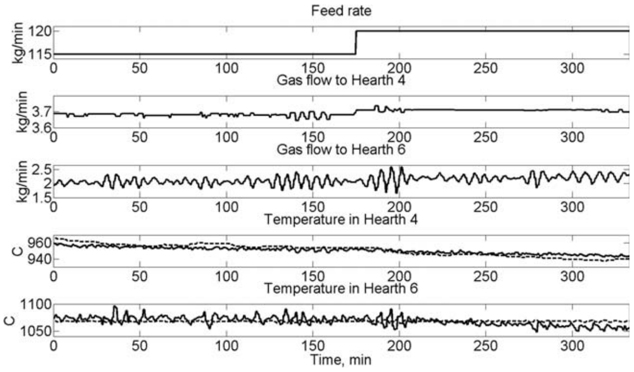

Figure 9. The model validation with the first feed rate step (the dashed lines in the temperature plots denote the measured values, and the solid lines denote the model prediction).

hearths observed from the mass distribution tests. When the solids enter the third hearth, their temperature rises rapidly and the dehydroxylation reaction begins. The metakaolin formation reaction lasts until the second half of the fifth hearth, by which time the solids temperature becomes increasingly get higher. The "spinel phase" or the product starts to be produced in the middle of the sixth hearth, since the solids temperature is high enough. Now, the exothermic reaction increases the temperature even faster and also the endothermic mullite formation reaction begins and leads to a cooling of the solids. From the beginning of the seventh hearth, the solids temperature decreases until the material exits the furnace at 750°C having a mullite content of approximately 5 mass-percent.

Next, the dynamic model was validated using the industrial data. Figure 8 presents the comparison of the gas phase temperatures next to the walls in different hearths between the model estimate and the industrial measurement data. In Hearth 6, the higher variability of the simulated temperature when compared with the measured one can be explained by the fact that the actual plant runs in a closed-loop and the temperature in Hearth 6 is controlled, whereas the model is run as an open-loop simulation.

Furthermore, two cases of feed rate step were used to validate the model dynamics. The recorded feed rate and the gas flows to the Hearths were used as the model inputs, and the model prediction of the temperature in the key Hearths 4 and 6 were compared with the measured values. In the first case, presented in Figure 9, the feed rate was increased from 115 kg/min to 120 kg/min, whereas the average gas flow to Hearths 4 and 6 raised from 3.68 kg/min to 3.71 kg/min and 2.05 kg/min to 2.21 kg/min, respectively. In fact, the control strategy keeps the gas temperature profile variations small during the transition. In the result, the gas temperature in Hearth 4 dropped from 960°C to 940°C, whereas the temperature in Hearth 6 is not affected by the transition much. As it can be seen from Figure 9, the model prediction follows the measured temperature in the key Hearths 4 and 6. In the second case, presented in Figure 10, the feed rate was increased from 115 kg/min to 120 kg/min, whereas the gas flow supply to Hearth 4 increases from 3.58 kg/min to 3.70 kg/min. The temperature in Hearths 4 and 6 was kept stable during the transition, and the simulated temperature accurately followed the measured values. As the validation results show, the model is able to produce good estimates of the current gas phase temperature and the model performance can be evaluated as satisfactory.

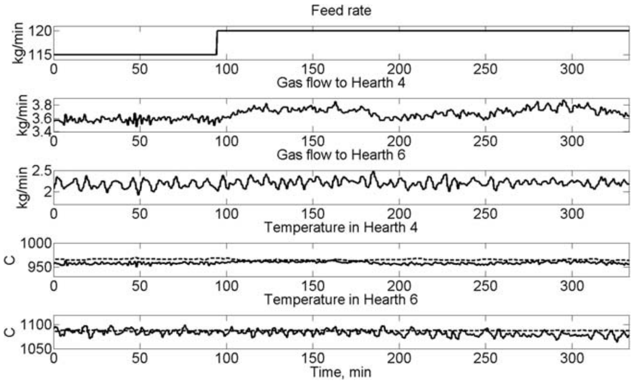

Figure 10. The model validation with the second feed rate step (the dashed lines in the temperature plots denote the measured values, and the solid lines denote the model prediction).

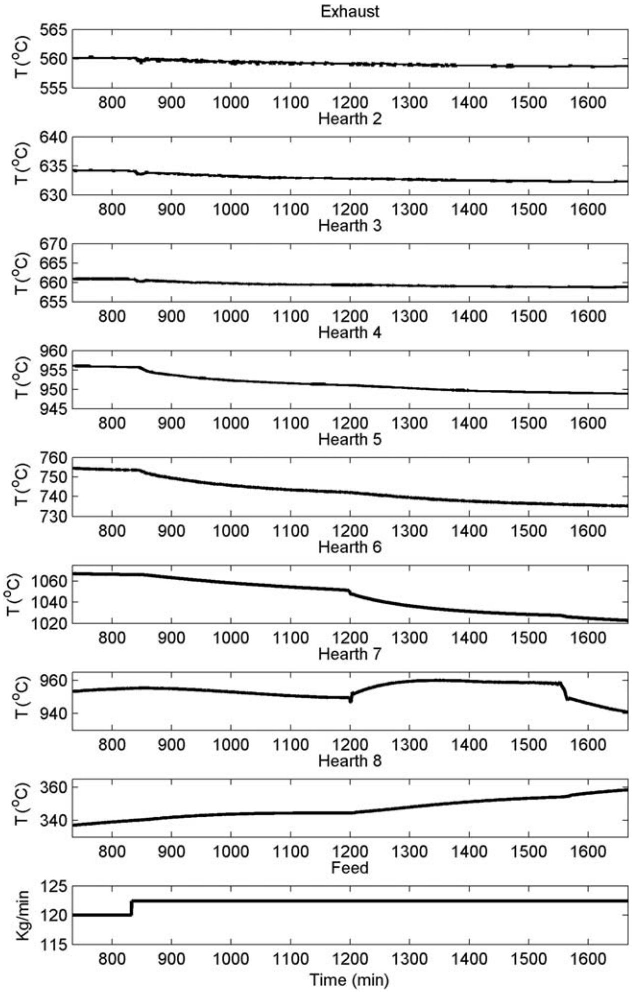

Figure 11. The response of the gas phase temperature next to the wall in the feed rate increase test.

Dynamic Behavior of the MHF

The dynamic behavior of the model was investigated to study the effect of the process inputs on the reactions

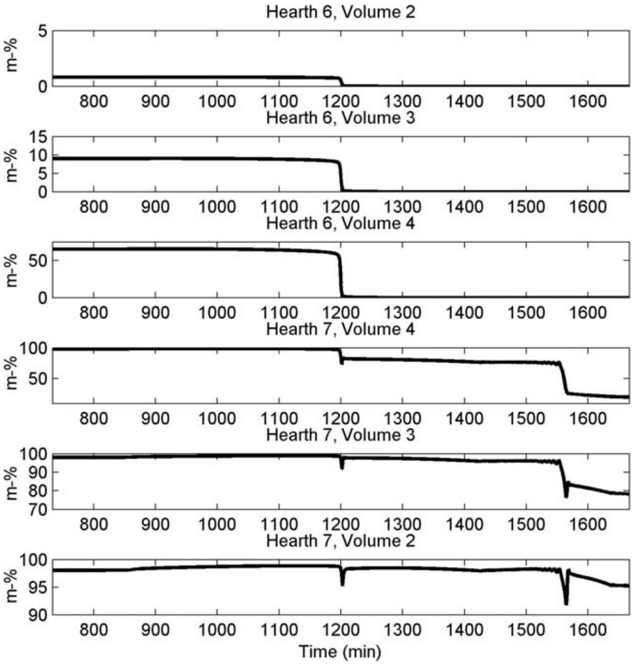

Figure 12. The response of the product content of the solid bed in Hearths 6 and 7 during the feed rate increase test.

occurring in the solid bed and the process outputs. Feed rate and the gas and air flows to Hearth 4 were chosen as manipulated variables while studying changes in the gas temperature profile through the furnace, and the quality variables: product and offspec mass-percentage in the lower hearths. The model response was studied by introducing a step change at 833 min in the input variables when the model had settled into a steady operation mode. In addition, Supporting Information Appendix C presents the results of the tests in which the gas and air flow rates to Hearth 6 were manipulated in a similar way.

Furnace response under feed rate changes

The model behavior was first studied by introducing a 2.4 kg/min (2%) step increase in the feed rate. At the beginning, the mullite formation in Hearth 7 slows down, which can be observed as the slight increase in the amount of the spinel phase in the final product, see Figure 12.

As the product formation reaction is not receiving enough heat, it collapses in the volumes of Hearth 6 at around 1200 min and the product contents in the Hearth drops to zero, as can be seen in the product content dynamics displayed in Figure 12. Thus, the product formation reaction moves to the beginning of Hearth 7. The shift of product formation to the beginning of Hearth 7 also affects the gas temperature profile in Hearths 5, 6, and 7 in Figure 11. However, the final product is still composed almost entirely of the spinel phase.

After 1560 min of the simulation time, the spinel formation partly moves to the middle of Hearth 7, which is confirmed by Figure 12. As a result, the metakaolin conversion to the spinel phase is not complete and the gas temperature in Hearth 7 decreases rapidly. During the whole test, the temperatures of the exhaust and the gas phases on Hearths 2 to 4 decrease steadily until settling to a new steady state, as Figure 11 shows. In contrast, the gas temperature in Hearth 8 slowly increases as a result of the rising temperature of the solid that enters to the last hearth.

Next, a step decrease of 2.4 kg/min (2%) was introduced to the feed rate and the model response is shown in Figures 13 and 14. At the beginning, the mullite formation is activated in Hearth 7 due to the temperature rise, which can be seen as a decrease of the spinel phase contents in Figure 14.

After 1260 min of the simulation time, the spinel formation partly moves toward the middle of Hearth 6, as demonstrated by Figure 14. Simultaneously, the mullite formation in Hearth 7 increases rapidly and the share of off-spec in the final product rises above 5%, which is demonstrated in Figure 14. As a result, the gas temperature in Hearths 6 and 7 changes its dynamics as it is seen in Figure 13.

In this case study, the temperatures of the exhaust and the gas temperatures of Hearths 2 to 5 increase steady until reaching a new steady state, since more specific energy is supplied to the furnace.

Furnace response under gas and air flows changes on Hearth 4

Next, a 11.0 kg/min (5%) step increase was introduced to the gas and air flows to Hearth 4. The model response is

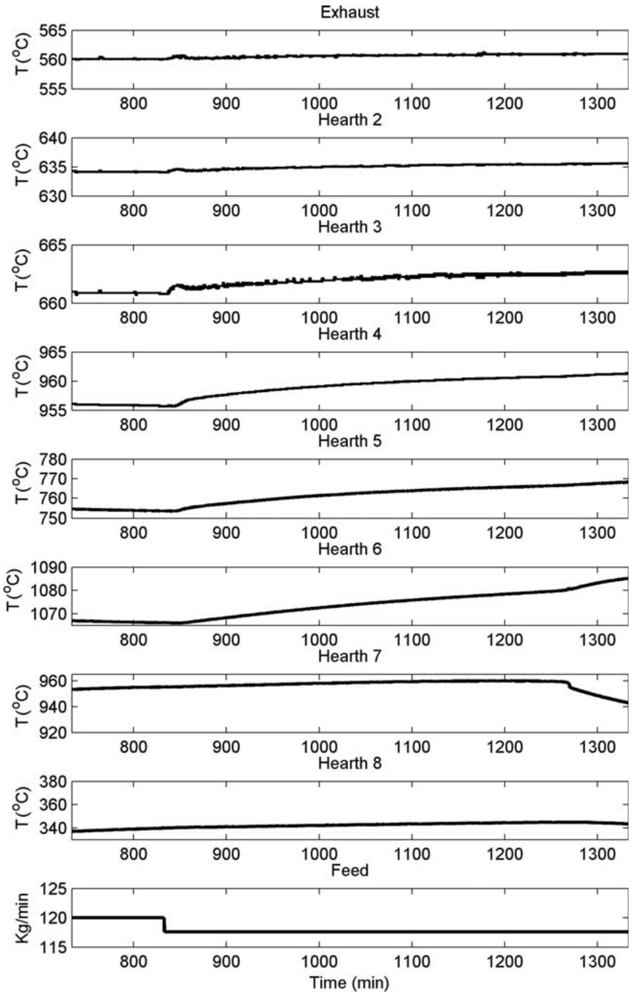

Figure 13. The response of the gas phase temperature next to the wall in the feed rate decrease test.

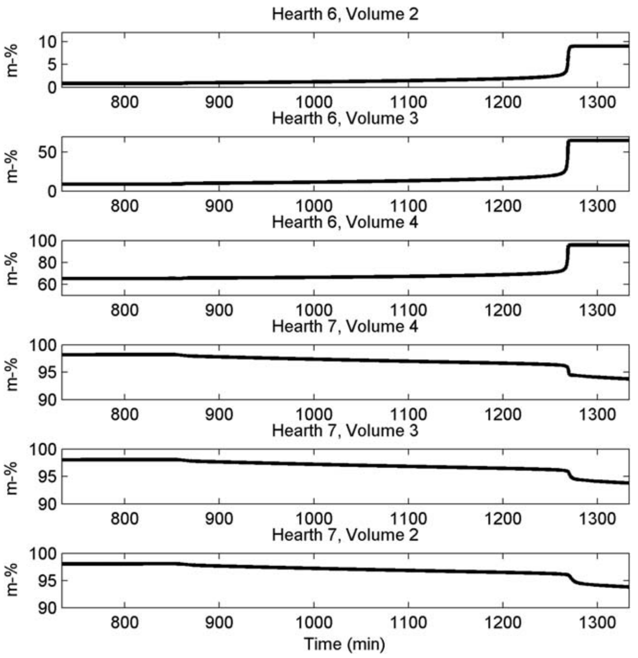

Figure 14. The response of the product content of the solid bed in Hearths 6 and 7 during the feed rate decrease test.

presented in Figures 15 and 16. At the beginning, the spinel phase formation in Hearth 6 and its conversion to mullite in Hearth 7 slowly increase their rates, as seen in Figure 16.

As the gas temperature on Hearth 6 rises, the product formation rapidly moves toward the earlier volumes at 1180 min, as it is demonstrated in Figure 16. It causes a small change in the dynamics of the gas temperature in Hearth 6. Simultaneously, the drop of the temperature in Hearth 7 is caused by the increased reaction rate of the endothermic mullite formation, which can be seen in Figure 16 as a decrease in the product content. The rise of the gas temperature in Hearth 8 before the 1180 minute of the simulation and its afterward decrease also follows the phenomena occurring in Hearth 7.

The exhaust gas temperature and the temperatures of Hearths 2, 3, and 4 increase instantly after the step change and afterward they settle to a higher steady state than the initial temperature was. As the extra energy is supplied to Hearth 4, the gas temperatures of Hearth 5 grows smoothly, which is caused by the slow increase of the temperature of the solid phase entering this hearth.

Subsequently, the model response was studied using a 11.0 kg/min (5%) step decrease in the gas and air flows to Hearth 4 and the results are shown in Figures 17 and 18. Due to the lack of energy supplied to the furnace, the product formation reaction first moves to the beginning of Hearth 7 at about 1130 min of simulation. At 1310 min, the reaction moves towards the middle of the hearth, as shown in Figure 18. Additionally, the gas phase temperature in Hearths 6 and 7 follow these reaction shifts, see Figure 17.

Next, the temperature in the solid phase drops, and does not achieve in any part of the furnace the temperature of 925°C required for the spinel phase reaction to occur. Thus, the reaction collapses around 1420 min, as observed in Figure 18. Now, the solid bed on Hearth 7 and the final product consist only of metakaolin. Since the reaction is not releasing heat anymore, it greatly affects the gas and solid temperature in the last three hearths of the furnace.

As the gas and air flow to Hearth 4 drops, the temperatures of the exhaust gas and Hearths 2, 3, and 4 decrease first with a steep drop and then more steadily until a new steady state is reached. In contrast, the temperature of Hearth 5 decreases steadily for the whole recorded time period.

A study of the model sensitivity to the reaction kinetics and the solid bed moving parameters

The performed step tests clearly demonstrate how sensitive the model is to the energy balance in the furnace: increasing or decreasing the feed rate by 2% without changing the supplied energy is able to substantially shift the temperature profiles. However, it seems that the model adequately describes the actual energy balance. On the other hand, in the mineral processing industry the mined material properties frequently vary. In order to demonstrate the sensitivity of the model to the reaction kinetics, simulations with the nominal inputs, specified in Table 5, were performed assuming doubled and halved frequency factors of the dehydroxylation, the product formation and the mullite formation reactions. The kinetics of the free water evaporation was not studied as the amount of free water in the feed stream is small. The changes of the gas

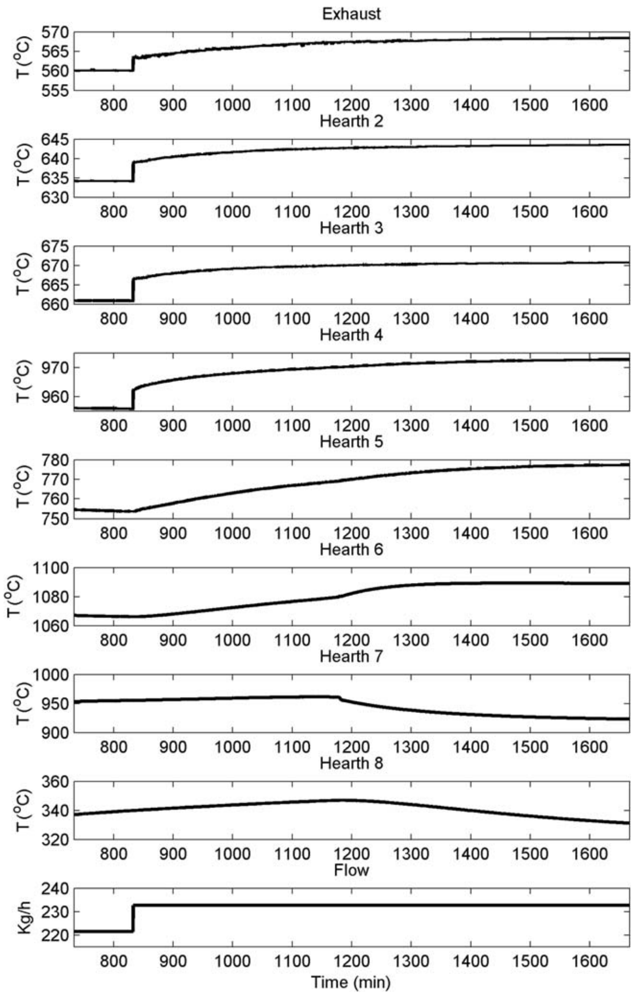

Figure 15. The response of the gas phase temperature next to the wall while increasing the gas and air flows to Hearth 4.

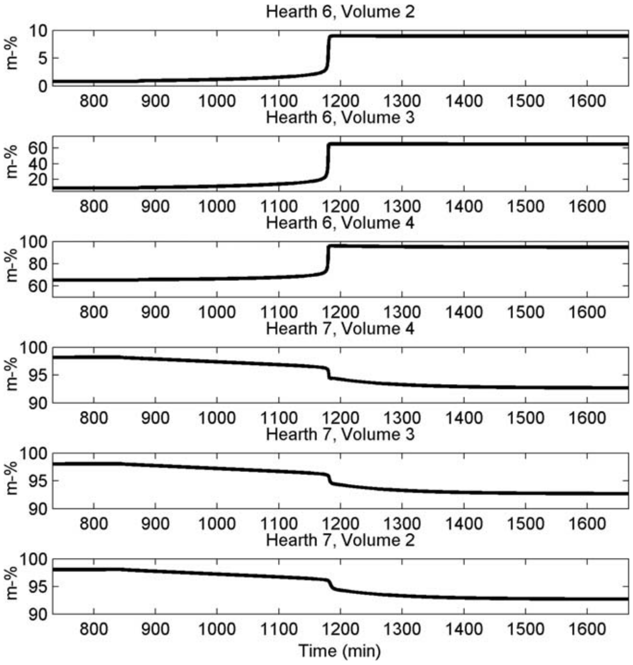

Figure 16. **The response of the product content in Hearths 6 and 7 while increasing the gas and air flows to Hearth 4.**

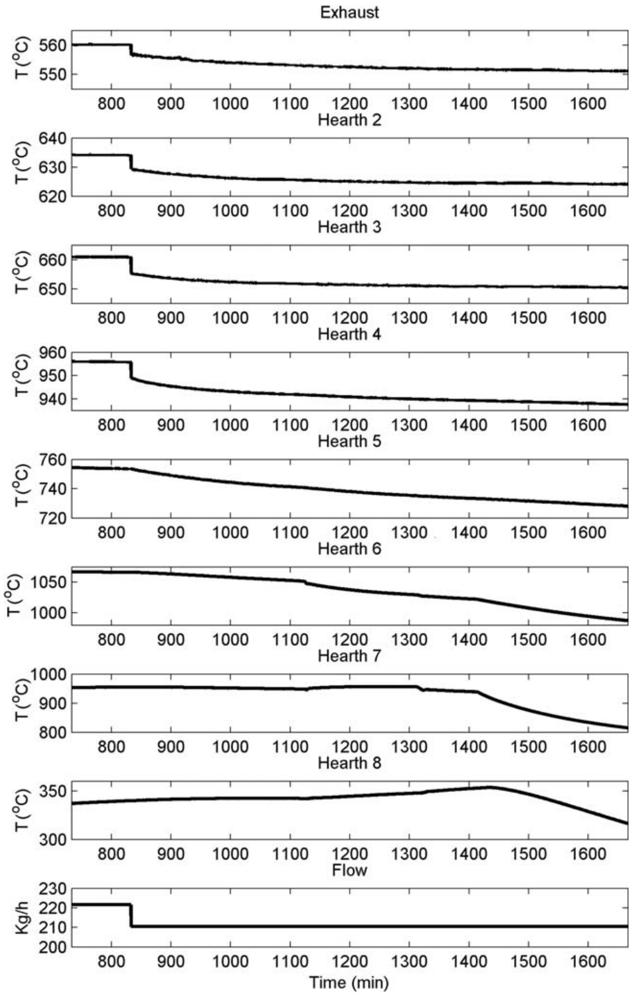

Figure 17. **The response of the gas phase temperature next to the wall while decreasing the gas and air flows to Hearth 4.**

and the solid phase temperature profiles are presented in Figure 19.

As the frequency factor of the dehydroxylation reaction increases, the temperature of both phases drops around Hearth 4, and rises around Hearth 6. The magnitude of the shift reaches its maximum for the solid phase temperature in Hearth 4, whereas the gas phase temperature and the temperature of the solid in Hearth 6 are not significantly affected. Thus, it can be concluded that estimating the dihydroxylation reaction kinetics based on available gas temperature profile measurements is difficult. Fortunately, the dehydroxylation reaction kinetics have a moderate effect on Hearths 6 and 7, which are especially critical for the process optimization and control.

The increase of the frequency of the product formation shifts the reaction to an earlier volume of Hearth 6, which significantly increases the temperature profile in Hearth 6 and greatly drops the temperature in the subsequent Hearths. In the result, the mass fraction of mullite in the final product increases by about 2.5%. On the other hand, the decrease of the frequency factor of the product formation does not shift the reaction, and therefore, the gas and the temperature profiles are only mildly affected. This can be explained by the exothermic nature of the product formation. Indeed, as the reaction activates in some volume of Hearth 6, the rising temperature maintains high reaction rate in this volume despite the decrease in the frequency factor. Overall, the kinetics of the product formation reaction is crucial for the process. Therefore, achieving efficient control and optimization has to be based on online monitoring of the product formation taking place in Hearth 6, as offline model tuning and parameter estimation would probably not be sufficient due to the importance of the phenomena.

The kinetics of the mullite formation does not affect the gas and temperature profiles through the furnaces, as confirmed by Figure 19 and the mullite content in the final product is changed by less than 1% in both cases.

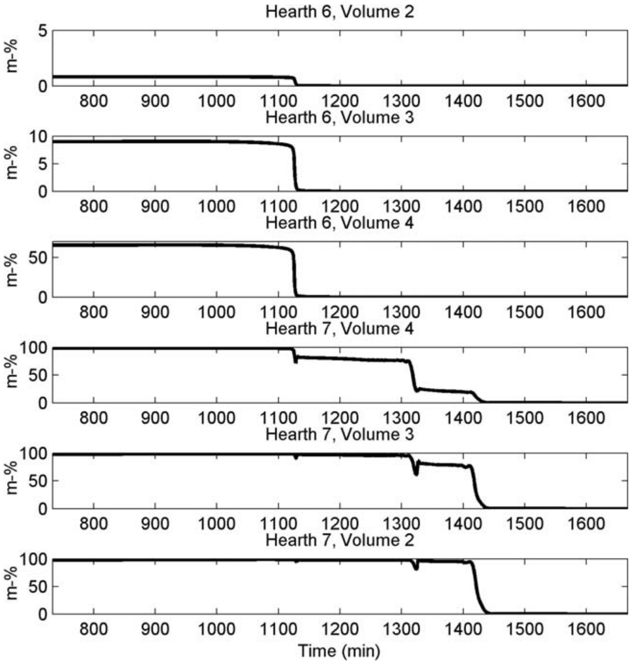

Figure 18. **The response of the product content in Hearths 6 and 7 while decreasing the gas and air flows to Hearth 4.**

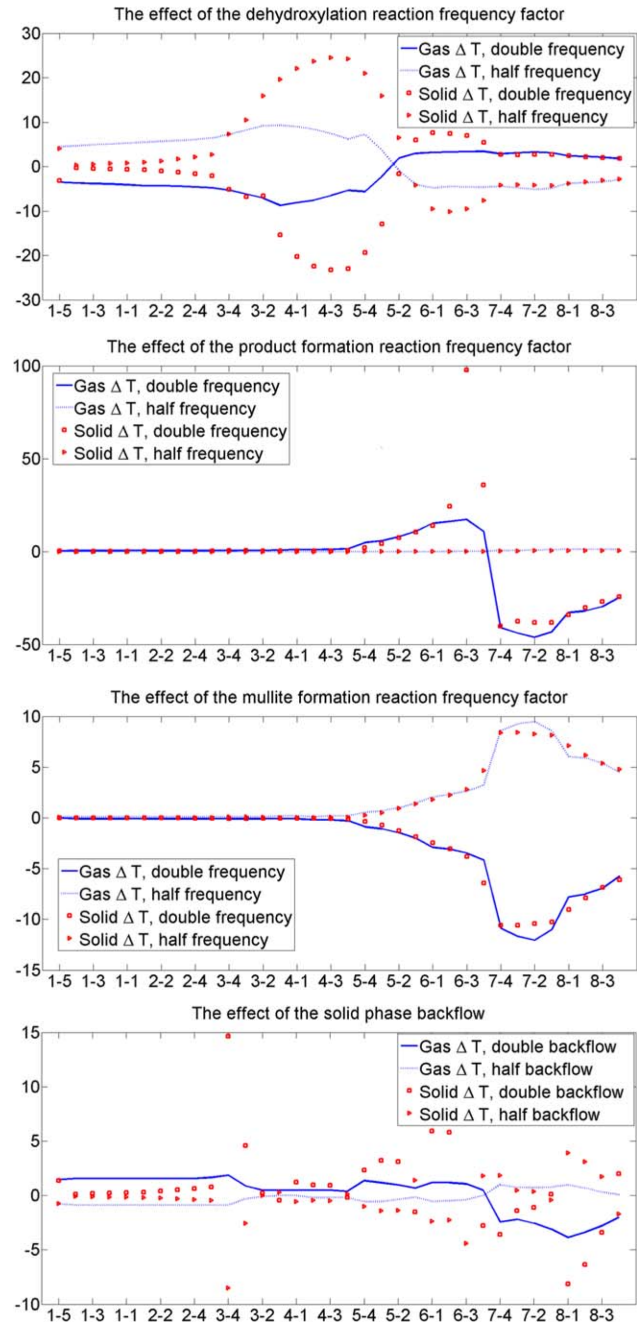

Figure 19. The change in the gas and solid temperature profiles due to change in the frequency factors of the reactions and the backflow in the solid phase movement.

[Color figure can be viewed in the online issue, which is available at wileyonlinelibrary.com.]

Regarding the dynamics of the solid phase, the backflow between the volumes in the hearths is difficult to estimate from the experiments. Thus, simulations were performed assuming the doubled and the halved backflow in Hearths 3 to 8. The backflow in Hearths 1 and 2 is small due to the short residence time in those hearths, and therefore, there is no need in its evaluation. The shift of the temperature profiles compared the results obtained using nominal parameters are presented in the last plot in Figure 19. It can be concluded that the intensity of the backflow has a relatively small effect on the furnace steady state.

Discussion of the Process Dynamics

The performed tests have demonstrated that the model outcomes are adequate. In particular, the spinel phase formation takes place in the last two volumes of Hearth 6 and first two volumes of Hearth 7, which agrees with the process knowledge. More specifically, the reaction moves towards the entrance of Hearth 6 when higher specific energy is supplied to the furnace, and the reaction shifts toward Hearth 7 as the amount of the supplied energy decreases. In the former case, higher temperature is reached in the solid phase which activates the mullite formation reaction in Hearth 7. On the other hand, if the specific energy is decreased too much, the temperature in the solid phase drops below the temperature required for spinel formation, and the reaction collapses. In this case, the output of the furnace consists of pure metakaolin. Thus, it can be concluded that the furnace must be controlled such a way as to direct the spinel formation at the end of Hearth 6 and the first volume of Hearth 7, which would deliver both highest content of the spinel phase in the product and stable operating conditions.

The dynamics of the temperature profile through the furnace is the result of complex interactions between the fast dynamics of the gas phase, the slower dynamics of the solid content and the even slower dynamics of the furnace walls. As an example, during the changes in the gas and air feed flows, the gas phase temperatures show first fast responses and then slow dynamics while settling to their new steady values. On the other hand, it takes a considerably longer time for the gas phase temperatures to react to steps in the feed rate. In some cases, significant shifts in the temperature dynamics occur after a much longer time, even after 700 min, which denotes the ability of the solid bed and the walls to act as a reservoir of huge amounts of heat.

Comparing the dynamics of different furnace hearths, it was noticed that the temperatures of the exhaust gases and Hearths 2, 3, and 4 show qualitatively simple behaviour. In contrast, the temperature of the gas phase in Hearths 5 to 8 depends on the process inputs in a more complex and nonlinear way. This is explained by the shifts in the spinel phase and mullite formation reactions through Hearths 6 and 7.

Conclusions

A dynamic model of kaolin calcination in a Multi Hearth Furnace (MHF) was developed in this paper. This model describes the physical-chemical phenomena taking place in the six furnace parts: the solid phase, gas phase, walls, cooling air, rabble arms, and the central shaft. A simple mixing model was proposed to describe the dynamics of the solid phase, and experiments with a pilot plant have been conducted to estimate the parameters of the mixing model.

Simulation studies have confirmed that the outcomes of the developed model are qualitatively adequate and its performance can be evaluated as fairly good. Thus, the model can be used to study the physicochemical phenomena occurring inside the furnace and it provides temperature profile through the hearths. In particular, the model behaviour was studied by introducing step changes in the three input variables: the feed rate, and the gas, and air flows to Hearths 4 and 6. A discussion regarding the observed process dynamics was provided. In addition, the model sensitivity to the reaction kinetics and the backflow in the solid bed movement was also discussed. In addition, as the simulation results have demonstrated, the conditions in different volumes in a hearth vary greatly, and a conclusion can be made that introducing the division into volumes is required to properly represent the actual chemical-physical phenomena. In the future work, the properties of the feed material will be considered in the model along with a more detailed study of the solid bed dynamics which will take into consideration the effect of the rabble arm configuration.

Acknowledgment

The research leading to these results has received funding from the European Union Seventh Framework Programme (FP7/2013-2016) under Grant Agreement No. 310645.

Notation

Roman letters

A = area, m^2
A_i = frequency factor for reaction i, 1/s
C_i = concentration of solid component i, kg
c_i = concentration of gas component, mol/m^3
D_i = solid bed movement matrix of hearth i
$E_{\mathrm{A},i}$ = activation energy of reaction I, kJ/kg
F = total gas flow, m^3
h = heat transfer coefficient, W/m^{2}K
j = number of the current hearth
k = number of the volume
k_i = reaction rate coefficient for reaction i, 1/s
m = mass, kg
n_i = moles of gas component i, mol
Q = heat, kJ
R = gas constant, =8.3145 J/molK
R_i = reaction rate for reaction i, kg/s
R_r = mass transfer rate from solids to gas phase, kg/s
T = temperature, K
t = time, s

Greek letters

ε = emissivity, radiative exchange ratio
σ = Stefan-Boltzmann-constant (=5.67 × 10^{-8} W/(m^{2}K^4))

Indices

g = gas
s = solid
w = wall
gs = gas-solid
gw = gas-wall
gshaft = gas-shaft
garms = gas-arms
sg = solid-gas
sw = solid-wall
wa = wall-ambient
wg = wall-gas
ws = wall-solid
shaft,cool = central shaft-cooling air
arms, cool = rabble arms-cooling air
c = convective heat transfer

Literature Cited

1. Thomas R, Grose D, Obaje G, Taylor R, Rowson N, Blackburn S. Residence time investigation of a multiple hearth kiln using mineral tracers. *Chem Eng Process*. 2009;48:950–954.
2. Murray HH. Clays. In: *Ullmann's Encyclopedia of Industrial Chemistry*. Weinheim: Wiley-VCH Verlag, 2005:203–235.
3. Jämsä-Jounela S-L. Current status and future trends in the automation of mineral and metal processing. *Control Eng Pract*. 2001;9:1021–1035.
4. Thomas R. High temperature processing of kaolinitic materials. PhD Thesis, Birmingham (UK): University of Birmingham, 2010.
5. Luyben WL. *Process modeling, simulation and control for chemical engineers*, 2nd ed. Singapore: McGraw-Hill, Inc., 1990:15–16.
6. Ogunnaike BA. *Process dynamics, modeling, and control*, 1st ed. New York: Oxford University Press, 1994:89.
7. Järvensivu M, Saari K, Jämsä-Jounela S-L. Intelligent control system of an industrial lime kiln process. *Control Eng Practice*. 2001;9:589–606.
8. Murray HH, Kogel JE. Engineered clay products for the paper industry. *Appl Clay Sci*. 2007;29:199–206.
9. Ptacek P, Soukal F, Opravil T, Noskova M, Havlica J, Brandstetr J. The kinetics of Al-Si spinel phase crystallization from calcined kaolin. *J Solid State Chem*. 2010;183:2565–2569.
10. Ptacek P, Soukal F, Opravil T, Halvica J, Brandstetr J. The kinetic analysis of the thermal decomposition of kaolinite by DTG technique. *Powder Technol*. 2011;208:20–25.
11. Langer AM. Evaluation of kaolinite and quartz differential thermal curves with a new high temperature cell. *Am Mineral*. 1967;52:509–523.
12. Castelein O, Soulestin B, Bonnet JP, Blanchart P. The influence of heating rate on the thermal behavior and mullite formation from a kaolin raw material. *Ceram Int*. 2001;27:517–522.
13. Gao Y, Glasser B, Ierapetritou M, Cuitino A, Muzzio F, Beeckman J, Fassbender N, Borghard W. Measurement of residence time distribution in a rotary calciner. *AIChE J*. 2013;59:4068–4076.
14. Ferron J, Singh D. Rotary kiln transport process. *AIChE J*. 1991;37: 774–758.
15. Meisingset HC, Balchen JG. Mathematical modeling of a rotary hearth coke calciner. *Model Identificat Control*. 1995;16:193–212.
16. Martins MA, Oliveira LS, Franca AS. Modeling and simulation of petroleum coke calcination in rotary kilns. *Fuel*. 2001;80:1611–1622.
17. Voglauer B, Jörgl HP. Dynamic model of a roast process for simulation and control. *Math Comput Model Dyn Sys*. 2004;10:217–230.
18. Liu X, Jiang J. Mass and heat transfer in a continuous plate dryer. *Drying Technol*. 2004;22:1621–1635.
19. Ginsberg T, Modigell M. Dynamic modelling of a rotary kiln for calcination of titanium dioxide white pigment. *Comput Chem Eng*. 2011;35:2437–2446.
20. DIPPR-801. Project 801, Evaluated Process Design Data, Design Institute for Physical Properties (DIPPR). American Institute of Chemical Engineers, 2012. Available at: http://www.aiche.org/dippr/events-products/801-database.
21. Perry RH, Green DW. *Perry's Chemical Engineering Handbook*. New York: McGraw-Hill, 1997.
22. Schieltz NC, Soliman MR. Thermodynamics of the Various High Temperature Transformations of Kaolinite. In: *Proceedings of the 13th National Conference on Clays and Clay Minerals*. New York: Pergamon Press, 1966:1–11.
23. Sheyndlin A. editor. *Emissivity properties of solid materials*. Moscow: Energy, 1974.
24. Emissivity. Available at: http://www.engineering.com/Library/ArticlesPage/tabid/85/ArticleID/151/Emissivity.aspx, accessed on December 23, 2013.
25. Table of emissivity of various surfaces. Available at: http://www-eng.lbl.gov/~dw/projects/DW4229_LHC_detector_analysis/calculations/emissivity2.pdf, accessed on December 23, 2013.
26. Lyons JW, Min HS, Parisot PE, Paul JF. Experimentation with a wet-process rotary cement kiln via the analog computer. *Ind Eng Chem Process Design Dev*. 1962;1:29–33.
27. Bellotto M, Gualtieri A, Artioli G, Clark SM. Kinetic study of the kaolinite-mullite reaction sequence. Part I: kaolinite dehydroxylation. *Phys Chem Miner*. 1995;22:207–214.
28. Criado JM, Ortega A, Real C, Torres de Torres E. Re-examination of the kinetics of the thermal dehydroxylation of kaolinite. *Clay Miner*. 1984;19:653–661.
29. Saikia N, Sengupta P, Gogoi PK, Borthakur P. Kinetics of dihydroxylation of kaolinin presence of oil field effluent treatment plant sludge. *Appl Clay Sci*. 2002;22:93–102.
30. Silva RA, Teixeira SR, Souze AE, Santos DI, Romero M, Rincon J. Nucleation kinetics of crystalline phases from a kaolinitic body used in the processing of red ceramics. *Appl Clay Sci*. 2011;52:165–170.
31. Ptacek P, Kreckova M, Soukal F, Opravil T, Havlica J, Brandstetr J. The kinetics and mechanism of kaolin powder sintering I. The dilatometric CRH study of sinter-crystallization of mullite and cristobalite. *Powder Technol*. 2012;232:24–30.
32. Gualtieri A, Bellotto M, Artioli G, Clark SM. Kinetic study of the kaolinite-mullite reaction sequence. Part II: mullite formation. *Phys Chem Miner*. 1995;22:215–222.

Manuscript received Dec. 5, 2014, and revision received May 27, 2015.